Materials and Design 195 (2020) 108958

Contents lists available at ScienceDirect

Materials and Design

journal homepage: www.elsevier.com/locate/matdes

Transient nucleation in selective laser melting of Zr-based bulk metallic glass

A. Ericsson [a,*], V. Pacheco [b], M. Sahlberg [b], J. Lindwall [c], H. Hallberg [a], M. Fisk [a,d]

[a] Division of Solid Mechanics, Lund University, PO Box 118, SE 22100 Lund, Sweden
[b] Department of Chemistry, Ångström Laboratory, Uppsala University, Box 523, SE 75120 Uppsala, Sweden
[c] Mechanics of Solid Materials, Luleå Technical University, SE 97187 Luleå, Sweden
[d] Materials Science and Applied Mathematics, Malmö University, SE 20506 Malmö, Sweden

HIGHLIGHTS

- Crystallization in SLM processing of AMZ4 is predicted using a transient nucleation model based on CNT.
- The nucleation rate is shown to depend on the heating/cooling rate of the temperature cycles in SLM.
- A diminishing volume fraction is observed at laser powers below 80 W, in agreement with XRD analysis of SLM processed AMZ4.
- The results suggest that transient nucleation effects play a critical role in promoting glass formation in SLM.

GRAPHICAL ABSTRACT

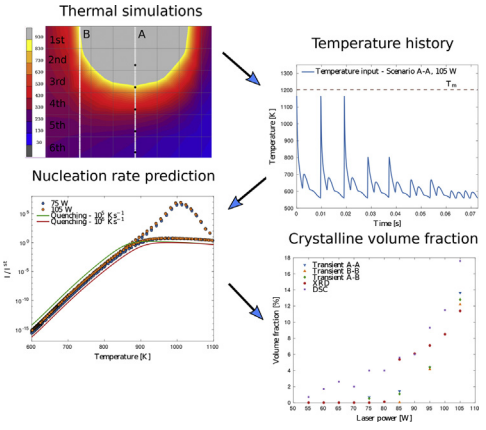

ARTICLE INFO

Article history:
Received 2 March 2020
Received in revised form 18 June 2020
Accepted 4 July 2020
Available online 15 July 2020

Keywords:
Additive manufacturing
Selective laser melting
Metallic glass
Crystallization
Classical nucleation theory
Transient nucleation

ABSTRACT

The crystallization rate during selective laser melting (SLM) of bulk metallic glasses (BMG) is a critical factor in maintaining the material's amorphous structure. To increase the understanding of the interplay between the SLM process and the crystallization behavior of BMGs, a numerical model based on the classical nucleation theory has been developed that accounts for the rapid temperature changes associated with SLM. The model is applied to SLM of a Zr-based BMG and it is shown that the transient effects, accounted for by the model, reduce the nucleation rate by up to 15 orders of magnitude below the steady-state nucleation rate on cooling, resulting in less nuclei during the build process. The capability of the proposed modelling approach is demonstrated by comparing the resulting crystalline volume fraction to experimental findings. The agreement between model predictions and the experimental results clearly suggests that transient nucleation effects must be accounted for when considering the crystallization rate during SLM processing of BMGs.

1. Introduction

Bulk metallic glasses (BMG) is a class of materials with remarkable properties such as high tensile strength, raised elastic strain limit, high hardness and resilience, improved corrosion resistance and tunable

* Corresponding author.
E-mail address: anders.ericsson@solid.lth.se (A. Ericsson).

https://doi.org/10.1016/j.matdes.2020.108958

magnetic properties [1,2], which makes them suitable for a wide range of engineering applications such as spring materials, pressure sensors, precision tools and biomedical implants [1,3,4]. Fabrication of BMGs can be achieved through cooling from the liquid state at a sufficiently high cooling rate, typically in the order of $10^1 - 10^3$ Ks^{-1}, suppressing nucleation of crystalline phases in favor of an amorphous atomic structure [3]. The localized laser processing utilized in additive manufacturing (AM) by selective laser melting (SLM) enables the possibility to quickly melt and dissipate heat from the material during processing and provides a promising method to produce BMGs without geometrical restrictions on the manufactured part [5–7]. However, issues arise as the local laser processing leads to complex temperature histories in the fused material. The repeated deposition of layers during the build process implies reheating of previous layers, which can cause crystallization to occur in the heat affected zone (HAZ) [5,6,8,9]. On the other hand, localized partial crystallization can be desirable, as it can promote ductility in the otherwise intrinsically brittle material, resulting in a BMG-crystalline composite. The improved ductility has been shown to depend on the size, shape, distribution and volume fraction of the dispersed crystalline inclusions, factors which in turn are the results of the thermal history experienced by the material [10–13]. Accurate prediction and control of the crystallization process under the complex temperature histories involved in AM by SLM is therefore of great interest.

Several approaches to model the crystallization process during laser processing of BMGs have been proposed. Vora et al. [14] compared the temperature history from a thermal finite element (FE) model of laser processing with an experimentally determined time-temperature-transformation (TTT) diagram. Lu et al. [15] proposed a similar technique, in which continuous-cooling-transformation (CCT) and continuous-heating-transformation (CHT) diagrams were generated using empirical relationships for the critical heating and cooling rate from differential scanning calorimetry (DSC) measurements. In both cases, comparison between the transformation diagrams and the thermal histories allowed a qualitative identification of the HAZ region in the material, where crystallization was most likely to occur. However, such transformation diagrams are only valid under the conditions at which they were obtained. Hence, the aforementioned approaches can, therefore, not be used to quantitatively predict the crystalline volume fraction during multiple heating/cooling cycles. For such predictions, it is necessary to describe the underlying physics of the crystallization process and distinguish between the mechanisms of nucleation and growth with respect to the temperature history experienced by the material.

Classical nucleation theory (CNT) is a useful method to model nucleation in various materials and processes [16–19]. Shen et al. [20] employed CNT to model the crystallization process during laser processing of a BMG and demonstrated the importance of treating the temperature dependence of the nucleation and growth rate seperately. This was manifested by the observation that certain regions in the material experienced different temperature histories and thus different degrees of nucleation and growth. The HAZ was identified as the region where significant nucleation, followed by growth, took place during reheating. However, they assumed that nucleation occured under steady-state conditions, implying that the nucleation rate is constant. This is a fair approximation in many applications but has been shown to be incorrect when nucleation proceeds under rapid cooling or heating of the material [13,21–25], such as in the case of SLM processing of metallic materials.

In the present work, we model the process of nucleation and growth of crystals from the supercooled liquid state using a CNT model that accounts for transient nucleation effects due to rapid temperature changes. The model is calibrated using an experimentally determined TTT-diagram of AMZ4, a bulk metallic glass that comprises Zr, Cu, Al and Nb ($Zr_{59.3}Cu_{28.8}Al_{10.4}Nb_{1.5}$ (at%)). Considering temperature variations from thermal FE simulations of a SLM process, the crystallization across the build direction is analysed for different laser powers and compared with experimental results. It is demonstrated that transient nucleation effects cannot be neglected when modelling the crystallization rate during SLM processing of BMGs.

2. Experimental procedure

Samples of AMZ4 were produced by SLM from commercially available powder using an EOS M290 [26]. The amorphous structure of the printed samples was investigated by X-ray diffraction [27].

The crystallization of AMZ4 at different temperatures was investigated using thermal analysis. Two different DSC techniques were employed, conventional heat-flux DSC and Flash DSC. Conventional

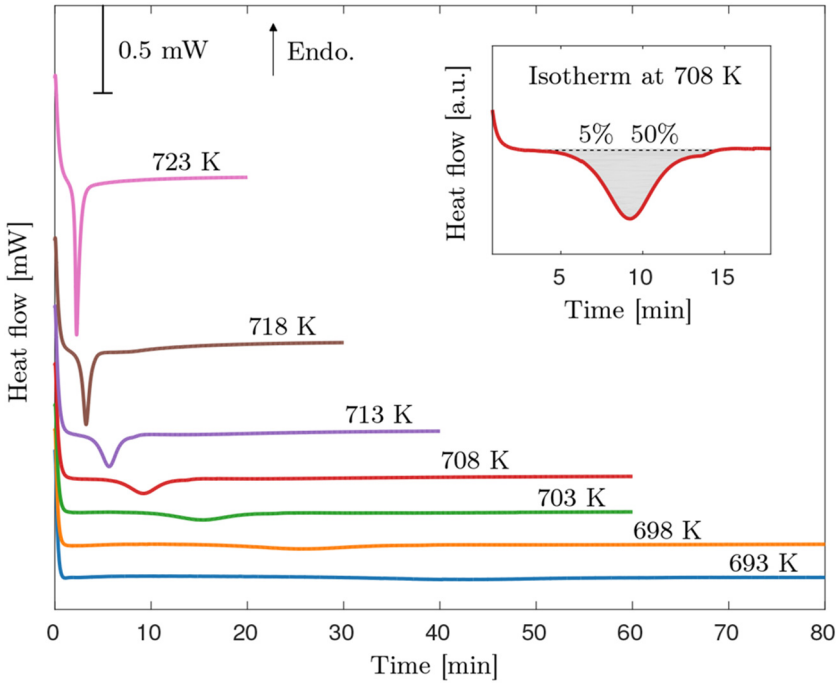

Fig. 1. Conventional DSC scans of AMZ4 at different temperatures (693–723 K). The exothermic peaks were integrated with respect to a horizontal baseline to obtain the crystalline volume fraction as a function of time. The inset shows the integration at 708 K.

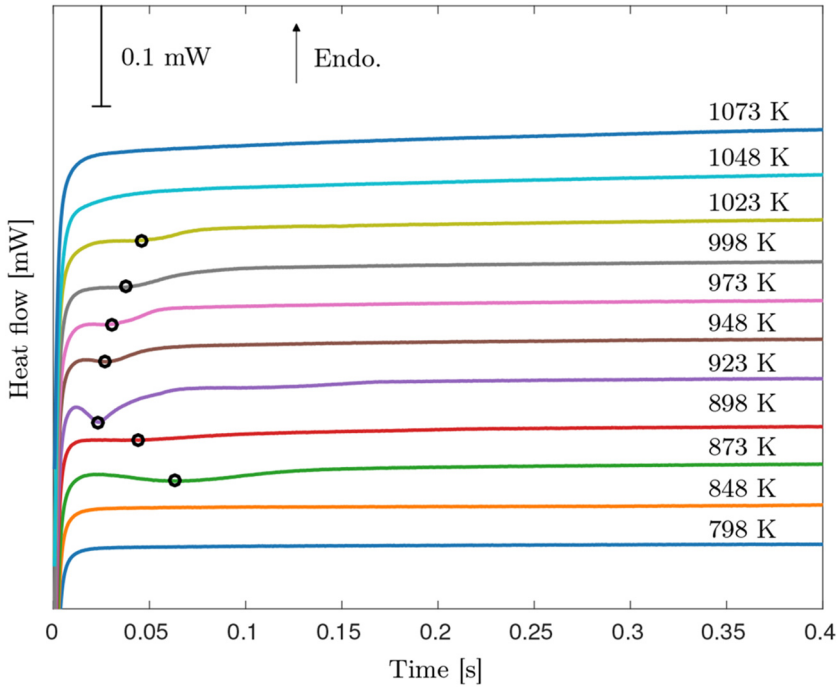

Fig. 2. Flash DSC scans of AMZ4 at different temperatures (798–1073 K). The crystallization events are marked with (◦).

heat-flux DSC was used to measure isothermal crystallization of the printed samples after heating from the glassy state (693–723 K). Conventional thermal analysis was conducted using a Netzsch 204F1 DSC. The samples were placed in aluminum crucibles, which were subsequently sealed inside an Ar-filled glove box with water and oxygen contents below 1 ppm. The samples were heated to the temperature of interest at a heating rate of 100 $\mathrm{Kmin^{-1}}$ after which the temperature was kept constant. Further details about the experimental procedure can be found in [27]. Fig. 1. shows the measured heat flow as a function of time at different temperatures. In order to obtain an estimate of the crystallized volume fraction as a function of time, the exothermic peaks were integrated with respect to a horizontal baseline as shown in the inset in Fig. 1. The time for 5, 50 and 100% crystallization was evaluated and serve as the lower part of the TTT-diagram appearing in Figs. 3 and 4.

Flash DSC was used to measure isothermal crystallization in the supercooled liquid region (798–1073 K). The Flash DSC technique has recently been recognised as a suitable tool to study phase transformations in BMGs [13,28,29]. The thermal analysis was conducted by Mettler Toledo using the Flash DSC2+ apparatus [30]. The sample size requirement was <30 μm, which limited the study to feedstock powder material. The AMZ4 powder was confirmed to be amorphous using XRD [31]. The samples of AMZ4 powder [26] were purged with Ar for 45 min at a flow rate of 80 ml $\mathrm{min^{-1}}$ with a sample support temperature of 233 K. The support temperature was then lowered to 193 K and the samples were heated until molten, followed by a quench to the temperature of interest at a cooling rate of $2 \cdot 10^4\,\mathrm{Ks^{-1}}$; after which the temperature was kept constant. The cooling rate of $2 \cdot 10^4\,\mathrm{Ks^{-1}}$ was sufficient to ensure that the material had not crystallized prior to reaching the target temperature. This was confirmed by performing cooling experiments from the molten state to room temperature with varying cooling rates between $1 \cdot 10^3 - 5 \cdot 10^4\ \mathrm{Ks^{-1}}$. Fig. 2 shows the measured heat flow as a function of time. Exothermic peaks corresponding to crystallization events are apparent at temperatures 873–1023 K, the maximum heat flow and the corresponding time for these peaks are marked in Fig. 2. The selection of a integration baseline could not be made with confidence for these measurements. Instead, the time for the peak values, marked in Fig. 2, serve as a conservative estimate of the TTT-diagram shown in Fig. 3.

3. Classical nucleation theory

This section briefly summarizes the classical nucleation theory. In CNT, the early stage of a phase transformation is assumed to occur by the formation of atomic clusters of the new phase. Following Kelton et al. [21,23,25], the change in energy required to form a cluster of n atoms can be expressed by

$$\Delta G(n) = n\Delta G' + (36\pi)^{1/3}\bar{v}^{2/3}n^{2/3}\sigma \tag{1}$$

where $\Delta G'$ is the change in Gibbs energy per atom, $\bar{v}$ is the average atomic volume and σ is the solid-liquid interfacial energy per unit area. Here $\Delta G'$ is negative and σ is positive, which implies that Eq. (1) is positive for small cluster sizes and reaches a maximum at a certain cluster size, refered to as the critical cluster size n^*, given by

$$n^* = \frac{32\pi\bar{v}^2\sigma^3}{3|\Delta G'|^3} \tag{2}$$

Clusters smaller than n^* are called embryos and have a higher probability to dissolve, while clusters larger than n^* are called nuclei and are likely to grow to macroscopic sizes. At the critical cluster size, the new phase is in unstable equilibrium with the surrounding initial phase.

The classical nucleation theory provides a theoretical description of the rate at which clusters grow from pre- to postcritical size. It is assumed that clusters of n atoms, with the configural state E_n, grow or shrink by the addition or loss of a single atom; of state E_1. As discussed in [21,23,32], this leads to a series of bimolecular reactions of the form

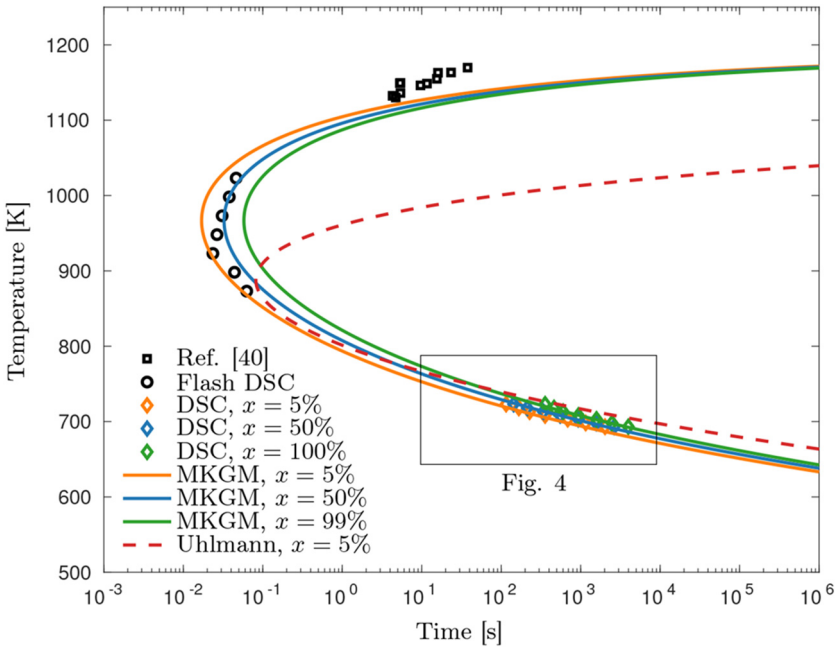

Fig. 3. Calculated TTT-diagram at different crystalline volume fractions using the MKGM model (solid lines), Uhlmann's model (red dashed line) and experimentally estimated data points from DSC measurements (◦ Flash DSC, ⋄ DSC) as described in section 2. The measurements reported by Heinrich et al. [40] have also been included for reference (□). A magnification of the lower temperature part is shown in Fig. 4.

$$E_{n-1} + E_1 \underset{k^-(n)}{\overset{k^+(n-1)}{\rightleftarrows}} E_n$$
$$E_n + E_1 \underset{k^-(n+1)}{\overset{k^+(n)}{\rightleftarrows}} E_{n+1} \tag{3}$$

where $k^+(n)$ is the rate of addition of single atoms to a cluster of size n and $k^-(n)$ is the rate of loss of single atoms from the same cluster.

In the case of nucleation in condensed matter, and as shown in [21,23,33], the forward rate constant $k^+(n)$ and the backward rate constant $k^-(n)$ can be estimated using transition state theory to provide

$$k^+(n) = O(n)\gamma \exp\left(-\frac{\delta G(n)}{2k_B T}\right)$$
$$k^-(n+1) = O(n)\gamma \exp\left(+\frac{\delta G(n)}{2k_B T}\right) \tag{4}$$

where $O(n)$ is the number of possible attachment sites for a cluster of n atoms, with $O(n) \approx 4n^{2/3}$ for a spherical cluster, $\delta G(n)$ is the energy difference between a cluster of $n+1$ and n atoms, i.e. $\delta G(n) = \Delta G(n+1) - \Delta G(n)$, k_B is the Boltzmann constant and T is the absolute temperature. The parameter γ is an atomic jump frequency at the cluster interface, often assumed to be the same as the jump frequency governing bulk diffusion in the parent phase, i.e.

$$\gamma = \frac{6D}{\lambda^2} \tag{5}$$

where D is an effective diffusivity and λ is the jump distance [25].

Based on the kinetic model in Eq. (3) the evolution of the time dependent cluster size distribution $N(n,t)$, representing the number of clusters per unit volume of size n at time t, can be described by a set of coupled differential equations

$$\frac{\partial N(n,t)}{\partial t} = N(n-1,t)k^+(n-1) - N(n,t)\left(k^+(n) + k^-(n)\right) + N(n+1,t)k^-(n+1) \tag{6}$$

which can be written in terms of the nucleation rates of cluster sizes $n-1$ and n, expressed as

$$\frac{\partial N(n,t)}{\partial t} = I(n-1,t) - I(n,t) \tag{7}$$

where the time dependent and size-dependent nucleation rate $I(n,t)$ (number of clusters per unit volume and time), is defined as

$$I(n,t) = N(n,t)k^+(n) - N(n+1)k^-(n+1) \tag{8}$$

The nucleation rate is often treated as a time-independent quantity, which implies that a convenient analytical expression of the steady-state nucleation rate can be derived from Eq. (8). This approach is briefly discussed in the succeeding section.

3.1. Steady-state nucleation

Numerical solutions of the differential equations in Eq. (6), assuming isothermal conditions, have shown that the cluster size distribution evolves in time until it eventually approaches a steady-state distribution [21]. The nucleation rate provided by Eq. (8) then becomes independent of the cluster size and time, i.e. $I(n,t) = I^{st} = \text{constant}$. A well-known expression for the steady-state nucleation rate was analytically derived from Eq. (8) in [32,34] and is usually expressed as

$$I^{st} = Zk^+(n^*)N^{eq}(n^*) \tag{9}$$

where Z is the Zeldovich factor, $k^+(n^*)$ is the forward rate constant evaluated at the critical cluster size and $N^{eq}(n^*)$ is the equilibrium cluster size distribution also evaluated at the critical size. The Zeldovich factor is given by

$$Z = \left(\frac{|\Delta G'|}{6\pi k_B T n^*}\right)^{1/2} \tag{10}$$

and the equilibrium cluster size distribution is expressed as

$$N^{eq}(n) = N_0 \exp\left(-\frac{\Delta G(n)}{k_B T}\right) \tag{11}$$

where N_0 is the initial number of atoms per unit volume in the system [25,32,34].

By making use of the steady-state nucleation rate I^{st}, the associated steady-state cluster size distribution N^{st} can be evaluated from Eq. (8), to obtain [21,25].

$$N^{st}(n) = N^{eq}(n) I^{st} \sum_{m=n}^{\tilde{v}} \frac{1}{N^{eq}(m) k^+(m)} \tag{12}$$

where $\tilde{v}$ is an upper cluster size limit, which has to be chosen such that $\Delta G(\tilde{v})$ is at least $k_B T$ lower than the energy at the critical cluster size, $\Delta G(n^*)$. At cluster sizes larger than $\tilde{v}$ it is assumed that $N^{st}(n) = 0$.

The analytical expression of the steady-state nucleation rate in Eq. (9) has been formulated to account for the transient time until steady-state conditions are obtained. Although several analytical solutions exist, the most frequently used form, discussed in [21,25], is expressed as

$$I(t) = I^{st} \exp\left(-\frac{\tau}{t}\right) \tag{13}$$

where τ is a characteristic relaxation time, related to the time it takes for clusters to grow through the critical region around n^*. It is important to note that Eq. (13) is derived for isothermal conditions and that the relaxation time τ is strongly dependent on the initial cluster size distribution [21]. Hence, application of Eq. (13) to nonisothermal conditions is difficult as it might lead to involved expressions for the relaxation time τ. As an alternative, numerical models of nucleation offer greater flexibility since they can be applied to model transient nucleation under nonisothermal temperature histories. This approach is discussed in the next section.

4. Numerical treatment of transient nucleation

To facilitate the numerical treatment, the coupled differential equations in Eq. (6) can be written in matrix form as

$$\frac{d\mathbf{N}}{dt} = \overline{\mathbf{K}}\mathbf{N} \tag{14}$$

where $\mathbf{N}$ is the time dependent cluster size distribution, appearing as

$$\mathbf{N} = \begin{bmatrix} N(\tilde{u}, t) \\ N(\tilde{u}+1, t) \\ \vdots \\ N(\tilde{v}, t) \end{bmatrix} \tag{15}$$

and $\overline{\mathbf{K}}$ is a tridiagonal matrix containing the rate-constants $k^+(n)$ and $k^-(n)$, on the form [21].

$$\overline{\mathbf{K}} = \begin{bmatrix} -k^+(\tilde{u}) & k^-(\tilde{u}+1) & 0 & \cdots & 0 \\ k^+(\tilde{u}) & -\left[k^-(\tilde{u}+1) + k^+(\tilde{u}+1)\right] & k^-(\tilde{u}+2) & \cdots & 0 \\ 0 & k^+(\tilde{u}+1) & -\left[k^-(\tilde{u}+2) + k^+(\tilde{u}+2)\right] & \cdots & 0 \\ \vdots & \vdots & \vdots & \ddots & k^-(\tilde{v}) \\ 0 & 0 & 0 & k^+(\tilde{v}-1) & -\left[k^-(\tilde{v}) + k^+(\tilde{v})\right] \end{bmatrix} \tag{16}$$

where $\tilde{u}$ is a lower cluster size limit that has to be chosen under the same conditions as $\tilde{v}$, as discussed in relation to Eq. (12).

When solving Eq. (14), boundary conditions have been introduced at the upper and lower cluster size limits. At the lower limit, clusters of size $\tilde{u}$ can not dissolve into smaller clusters since $k^-(\tilde{u})$ has been assumed to be zero in the first entry of the diagonal in $\overline{\mathbf{K}}$. At the upper limit, clusters larger than $\tilde{v}$ are assumed to have a zero probability of dissolving and will continue to grow to macroscopic sizes. This is reflected by the fact that $k^-(\tilde{v}+1)$ has been omitted from the matrix $\overline{\mathbf{K}}$ in Eq. (16).

The exponential factor in the rate constants in Eq. (4), implies that the set of ordinary differential equations (ODEs) in Eq. (14) are stiff. Although explicit/implicit Euler or Runge-Kutta time-stepping algorithms can be used, they lead to either inefficiently short timesteps or reduced accuracy, especially if $\overline{\mathbf{K}}$ varies with respect to time. To adress these issues, a variable order solver is adopted, designed to handle stiff differential equations such as those in Eq. (14). The model is implemented in Matlab and the system of equations are solved in time using the ode15s solver from the Matlab ODE suite [35]. In each simulation, the upper and lower cluster size limits are chosen as $\tilde{u} = 1$ and $\tilde{v} = 1.5 \cdot n_{eval}$, respectively, where n_{eval} is the cluster size for evaluation of the nucleation rate. This value is chosen to be $r_{eval} = r_*^{T_{max}} + 0.5(k_B T_{max}/\pi\sigma)^{1/2}$ where $r_*^{T_{max}}$ is the critical cluster size, written in terms of its radius, evaluated at the maximum temperature of the simulation, T_{max}. Note that the cluster size in terms of number of atoms or radius are related by $n = 4\pi r^3/3\bar{v}$ at any given cluster size. These choices ensure that the conditions for $\tilde{u}$ and $\tilde{v}$, as discussed in relation to Eq. (12), are fulfilled and that the nucleation rate is always evaluated at cluster sizes larger than the critical cluster size at each temperature.

The nucleation rate is evaluated using Eq. (8) and the number of nuclei formed per unit volume is calculated by integration of the nucleation rate with respect to time, i.e. by numerical evaluation of

$$\hat{N}_i(t) = \int_0^t I_i(n_{eval}, t')dt' \tag{17}$$

At the end of each time interval i, the number of nuclei formed during the timestep is stored in an array and the radius of nuclei from previous timesteps are updated using a Langrange-like approach [36] that provides

$$r(t + \Delta t) = r(t) + u(r)\Delta t \tag{18}$$

where Δt is the timestep and $u(r)$ is the size-dependent growth rate, taken as

$$u(r) = \frac{16D}{\lambda^2}\left(\frac{3\bar{v}}{4\pi}\right)^{1/3} \sinh\left[\frac{\bar{v}}{2k_B T}\left(\Delta G_v - \frac{2\sigma}{r}\right)\right] \tag{19}$$

which implies that the growth is assumed to be of polymorphic nature. Further discussions on Eq. (19) can be found in [18,22].

The crystallized volume fraction as a function of time, $x(t)$, is evaluated using the Johnson-Mehl-Avrami-Kolmogrov (JMAK) equation [23,37–39], generally expressed as

$$x(t) = 1 - \exp\left(-\frac{4\pi}{3}\int_0^t I(\tau)\left[\int_\tau^t u(r(t'))dt'\right]^3 d\tau\right) \tag{20}$$

that can be rewritten into the discrete form

$$x(t) = 1 - \exp\left(-\frac{4\pi}{3}\sum_{i=1}^{m}\hat{N}_i(t)r_i(t)^3\right) \tag{21}$$

where $r_i(t)$ is the time dependent radius of each nuclei formed during timestep i and $\hat{N}_i(t)$ is the number density of such nuclei. These quantities can be obtained from Eqs. (17) and (18).

In a similar fashion, the average nucleus size as a function of time $\bar{r}(t)$ can be evaluated using the following expression [36].

$$\bar{r}(t) = \frac{\sum_i^m \hat{N}_i(t)r_i(t)}{\sum_i^m \hat{N}_i(t)} \tag{22}$$

which takes into account the existence of different numbers of nuclei of different sizes and average their combined size with respect to the total number of nuclei formed.

5. Properties of AMZ4

This section discusses the material properties used to adapt the model to AMZ4. Models and experimental data of the necessary thermodynamic and kinetic parameters are presented.

5.1. Gibbs energy

The heat capacity of the liquid and crystalline states of AMZ4 as functions of temperature have been measured and fitted to the Kubaschewski equations by Heinrich et al. [40]. Integration of the difference in heat capacity with respect to temperature yields an expression for the change in Gibbs energy from the undercooled liquid to the crystalline state per unit mole on the form

$$\Delta G_m(T) = \Delta H_m(T) - T\Delta S_m(T) \tag{23}$$

where $\Delta H_m(T)$ and $\Delta S_m(T)$ are the enthalpy and entropy per unit mole, respectively. These quantities can be expressed as

$$\begin{aligned}\Delta H_m(T) &= \Delta H_f - \frac{a-c}{2}\left(T_m^2 - T^2\right) + b\left(T_m^{-1} - T^{-1}\right) + \frac{d}{3}\left(T_m^3 - T^3\right)\\ \Delta S_m(T) &= \Delta S_f - (a-c)(T_m - T) + \frac{b}{2}\left(T_m^{-2} - T^{-2}\right) + \frac{d}{2}\left(T_m^2 - T^2\right)\end{aligned} \tag{24}$$

where T_m is the melting temperature, ΔH_f and $\Delta S_f = \Delta H_f/T_m$ are the enthalpy and entropy of fusion, respectively, and where a, b, c and d are the fitting parameters in the Kubaschewski equations. The parameters are summarized in Table 1. Dividing Eq. (23) by Avogadros constant, N_A, yields the change in Gibbs energy per atom

$$\Delta G'(T) = -\frac{\Delta G_m(T)}{N_A} \tag{25}$$

where the minus sign has been introduced since $\Delta G_m(T) > 0$.

Table 1
Thermodynamic parameters related to the expressions for the Gibbs energy, presented in Eq. (24). The parameters are obtained from [40].

T_m	1203 K
ΔH_f	$8.578 \cdot 10^3$ Jmol^{-1}
ΔS_f	7.131 Jmol^{-1}K^{-1}
a	$5.224 \cdot 10^{-4}$ Jmol^{-1}K^{-2}
b	$1.031 \cdot 10^7$ JKmol^{-1}
c	$6.230 \cdot 10^{-3}$ Jmol^{-1}K^{-2}
d	$-6.047 \cdot 10^{-7}$ Jmol^{-1}K^{-3}

5.2. Diffusivity

The effective diffusivity D, appearing in Eq. (5), is estimated using the Stokes-Einstein relationship, providing

$$D = \frac{k_B T}{3\pi\lambda\eta} \tag{26}$$

where η is the viscosity of the liquid [41,42]. This relationship has been shown to break down in the supercooled liquid regime for several glass forming alloys, including alloys in the Cu-Zr system. Instead, a powerlaw relationship, $D \propto \eta^{-\xi}$, shows better agreement with measurements [43–45]. However, obtaining the decoupling exponent, ξ, requires measurements of both the activation energy for diffusion and the viscosity of the liquid as a function of temperature, whereof the former has not been measured for AMZ4, at least to the author's knowledge. Thus the Stokes-Einstein relationship in Eq. (26) is tentatively adopted in the present work.

The viscosity of the liquid has been measured for AMZ4 by Hembree [46], above the melting temperature but also in the vicinity of the glass transition temperature. Measurements in the intermediate temperature range were deemed inaccessible. The lower and upper temperature measurements were fitted using two independent Vogel-Fulcher-Tamman (VFT) expressions, one for the high temperature data and one for the low temperature data. A single fit for the full temperature range was not possible using the VFT relationship. Several other empirical expressions have been proposed as alternatives to the VFT equation. One of the more recent being the Blodgett-Egami-Nussinov-Kelton (BENK) expression [47], which have been shown to provide a good fit for both the upper and lower temperature range, using only one fitting parameter. The BENK equation can be expressed as [47].

$$\begin{aligned}\eta &= \eta_0 \exp\left(\frac{E(T)}{T}\right)\\ E(T) &= E_\infty + T_A(qT_r)^z\Theta(T_A - T)\end{aligned} \tag{27}$$

where $q = 4.536$ and $z = 2.889$ are universal fitting constants, independent of alloy composition, $T_r = (T_A - T)/T_A$ is a reduced temperature, $\Theta(\cdot)$ is the Heaviside step function and E_∞ is a fitting parameter for the activation energy, approximated using the universal scaling temperature T_A by $E_\infty = 6.466T_A$. The universal scaling temperature has been demonstrated to be proportional to the glass transition temperature T_g by $T_A \approx 2.02T_g$, where the glass transition temperature is estimated to be $T_g = 667$ K for the present material [46]. Thus the only remaining parameter is the high temperature viscosity constant η_0, obtained by fitting Eq. (27) to the data provided by Hembree [46], resulting in $\eta_0 = 4.72 \cdot 10^{-5}$ Pas.

5.3. Interfacial energy

Several models have been proposed for the solid-liquid interfacial energy, σ, a quantity that is difficult to determine experimentally. Consequently, it is also difficult to validate the results from the different proposed models for σ. It is, however, widely accepted that the solid-liquid interfacial energy possess a strong dependence on both temperature and structure [48–50]. A recent study, based on atomistic simulations, has revealed an unusual temperature dependence of the solid-liquid interfacial energy in the Cu-Zr system [51]. The results indicate that the value of the interfacial energy increases as the temperature is decreased below the melting point. A similar prediction is obtained using the phenomelogical model by [52], here denoted as the Mondal-Kumar-Gupta-Murty (MKGM) model. The model assumes a hard sphere approximation of the nucleus and a surrounding monolayer as the interfacial region. The monolayer is assumed to possess a similar atomic packing as that of the crystalline nucleus but lacking a crystalline arrangement of atoms. The model can be reduced to the following analytical expression [52].

$$\sigma(T) = \left[\frac{P}{\rho\lambda}\frac{3\Delta G_v(T)}{32\pi}\left(\Delta G_d^m(T) - \Delta G_d^L(T)\right)\right]^{1/2} \quad (28)$$

where $\Delta G_v(T) = -\Delta G_m(T)/V_m$ is the change in Gibbs energy per unit volume, V_m is the molar volume, $\Delta G_d^m(T)$ is the activation energy for diffusion in the monolayer, $\Delta G_d^L(T)$ is the activation energy for diffusion in the liquid. Further, ρ, P are the planar atomic density and packing factor of the crystal, respectively. The activation energy for liquid diffusion is calculated using Eq. (26) by assuming an Arrhenius temperature dependence of the diffusivity, i.e. $\Delta G_d^L(T) = k_B T \ln(3\pi\nu\lambda^3\eta(T)/k_B T)$, where ν is the atomic vibration frequency ~10^{13}. In a similar manner, the activation energy for diffusion in the monolayer is estimated using $\Delta G_d^m(T) = k_B T \ln(3\pi\nu\lambda^3\eta_{Tg}/k_B T_g)$, i.e. the atomic movement in the monolayer is assumed to be similar to that of the amorphous phase. The parameters, η_{Tg} and $\alpha = P/\rho$, are taken as calibration parameters in the present work, and are found using DSC measurements on AMZ4 as further discussed in Section 6.

Another, more common, estimation of the interfacial energy is found by Uhlmann's model [53].

$$\sigma = 0.495\left(\frac{\Delta H_f}{V_m}\right)^{2/3}(k_B T_m)^{1/3} \quad (29)$$

which assumes that the interfacial energy is temperature independent. Combination of Eq. (29) with CNT has been reported to show a quantitative agreement with experimentally measured steady-state nucleation rates in glass forming systems [18]. Uhlmann's model is therefore selected as a reference model for comparison with the temperature dependent MKGM model, provided by Eq. (28).

5.4. Atomic parameters

The atomic parameters, λ, $\bar{v}$, N_0 and V_m are evaluated using the periodic table and data provided by the material supplier. The molar volume is calculated using $V_m = M/\rho_m = 11.54\ \text{cm}^3\text{mol}^{-1}$, where M and ρ_m are the molar mass and density of the alloy, respectively. The average atomic volume is estimated using $\bar{v} = V_m/N_A = 19.16\text{A}^3$, which provides an average of the bulk volume per unit atom. Using the average atomic volume, the initial number density of atoms is evaluated using $N_0 = 1/\bar{v} = 5.220{\cdot}10^{28}\ \text{m}^{-3}$. Finally, the average atomic jump distance is estimated to be $\lambda = 2\bar{r} = 3.320\,\text{A}$, where $\bar{r} = (3\bar{v}/(4\pi))^{1/3}$ is the average atomic radius, estimated by assuming a spherical shape for the average atomic volume. These estimations provided an atomic jump distance of reasonable magnitude, comparable to reported values of other Zr-based BMGs [54,55].

6. Model calibration

Using JMAK theory, the parameters η_{T_g} and $\alpha = P/\rho$ in Eq. (28) are calibrated by fitting the model to the TTT-diagram obtained from the experiments described in section 2. A steady-state nucleation and growth rate is assumed for the calibration. Under these conditions, the crystallized volume fraction $x(t)$, given by Eq. (20), may be written as

$$x(t) = 1 - \exp\left(-\frac{\pi I^{st} u_{max}^3 t^4}{3}\right) \quad (30)$$

where I^{st} is the steady-state nucleation rate given by Eq. (9) and u_{max} is the maximum growth rate. Eq. (30) can be used to calculate the time t (x) it takes to crystallize a certain volume fraction x by rewriting Eq. (30) as

$$t(x) = \left[-\frac{3}{\pi I^{st} u_{max}^3}\ln(1-x)\right]^{1/4} \quad (31)$$

The maximum growth rate is obtained by taking Eq. (19) to the infinite limit, which yields the following expression for the maximum growth rate

$$u_{max} = \frac{16D}{\lambda^2}\left(\frac{3\bar{v}}{4\pi}\right)^{1/3}\sinh\left[\frac{\bar{v}\Delta G_v}{2k_B T}\right] \quad (32)$$

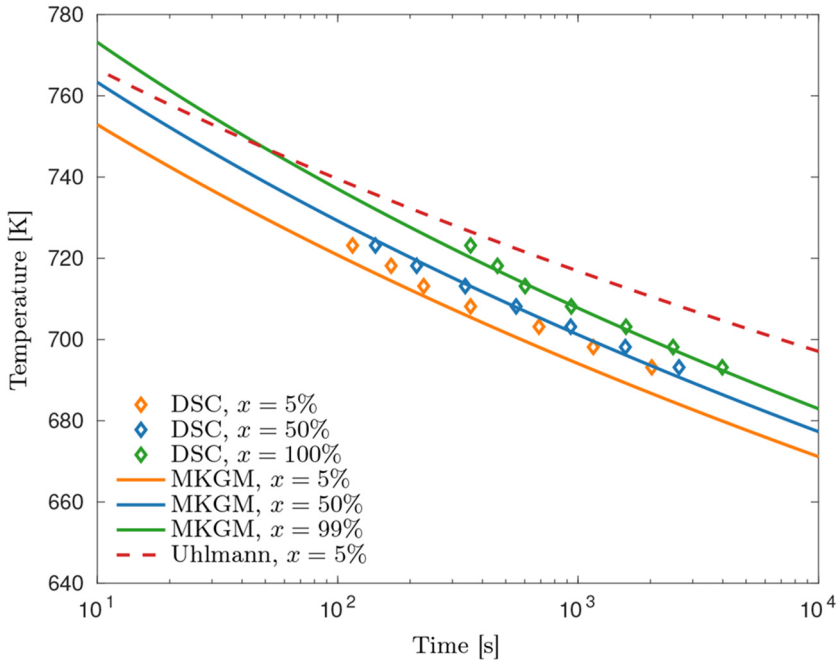

Fig. 4. A magnified image of the lower temperature region, indicated in Fig. 3, showing the agreement between the calculated TTT-diagram using the temperature dependent MKGM model (solid lines) and the DSC measurements (⋄) at different crystalline volume fractions. The calculated TTT-diagram using Uhlmann's model is also included as reference (red dashed line).

The calculated TTT-diagram based on the temperature dependent MKGM model for the interfacial energy, cf. Eq. (28), is shown in Fig. 3 for different crystalline fractions, $x(t)$, together with the DSC measurements (◦ Flash DSC, ⋄ DSC). The measurements reported by Heinrich et al. [40] have also been included for reference (□). A magnified plot of the lower temperature region is shown in Fig. 4. The agreement between the experimental data and the calculated TTT-diagram is good, especially at lower and intermediate temperatures where the calculated TTT-diagram coincides with the data from the experiments. For comparison, a calculated TTT-diagram, based on Uhlmann's model for the interfacial energy, cf. Eq. (29), has also been included in Figs. 3 and 4 (red dashed line). The diagram using Uhlmann's model agrees fairly well with the experiments at lower temperatures, especially considering that no parameters have been adjusted to fit the experimental data points. Comparing the two models, it is clear that the temperature dependent MKGM model provides a much closer resemblance with the measurements than Uhlmann's model. Not only is the diagram showing a better agreement with both the upper and lower temperature measurements, but the nose of the diagram coincides exactly with the Flash DSC measurements.

The calculated interfacial energies obtained from the calibrated MKGM model, Eq. (28), and from Uhlmann's model, Eq. (29), are shown in Fig. 5. The calibrated values of the MKGM model are $\eta_{Tg} = 1.5 \cdot 10^{16}$ Pas and $\alpha = P/\rho = 1.28$, respectively. The value of $\alpha = 1.28$ is comparable to calculated values for fcc Al of different atomic planes, i.e. $\alpha^{Al}_{(111)} = 0.82$, $\alpha^{Al}_{(100)} = 0.94$ and $\alpha^{Al}_{(110)} = 1.33$, cf. [52], and thus of reasonable magnitude. The calibrated value of $\eta_{Tg} = 1.5 \cdot 10^{16}$ Pas corresponds to the viscosity of the amorphous phase at room temperature, which in terms of the MKGM model translates into a high activation energy for diffusion in the monolayer. Considering that metallic glasses are known for their resistance to crystallization, it is quite expected that both of these parameters would obtain rather high values from the calibration as they increase the value of the interfacial energy.

It is important to remark that the actual crystallization process is likely to be much more complex than what is captured by the model. AMZ4 is an industrial grade alloy, made from a pre-alloy of Zr-Nb containing a high amount of impurities with a content of O up to 10300 ppm, H of up to 4540 ppm, N up to 1630 ppm, C up to 3810 ppm as well as Fe and Cr up to 3280 ppm [40,56,57]. Especially oxygen is known to deteriorate the glass forming ability of Zr-based glasses [57–59], causing the glass to initially crystallize as oxygen-induced compounds, which act as heterogeneous nucleation sites for further crystallization [57,58,60]. Hence, it is likely that heterogeneous nucleation has, to some extent, occured in the specimen. This phenomena is not accounted for in the present model. Another discrepancy is the observation that Zr-Cu-Al based bulk metallic glasses often crystallize into intermetallic compounds of different composition than the parent phase, e.g. $Zr_2(Al,Cu)$ [11,61–63]. Compositional differences between the matrix and the nuclei have been shown to alter the nucleation barrier and growth behavior of the nucleus significantly [64]. Although none of these effects have been included in the present model, it is striking how well the calibrated TTT-diagram agree with the experimental data, emphasizing a dominant temperature dependence of the interfacial energy.

7. Simulations of transient nucleation

The transient nucleation model described in Section 4 is employed in simulations of nucleation during non-isothermal phase transformations. First, the case of an initial liquid subjected to quenching at a constant cooling rate is presented. Different cooling rates are studied and the conditions under which transient nucleation becomes important for the present material is investigated. Second, simulations of nucleation during AM is presented, in which temperature histories obtained from thermal FE simulations of SLM is used as model input. SLM process parameters of AMZ4 as presented in [31] are adopted and the crystallization across the build direction is analysed and compared with experimental results from the XRD, DSC and scanning electron microscope (SEM) analyses in [31]. For both of the investigated scenarios, the results from the transient simulations are compared with results considering steady-state nucleation rates using Eq. (9).

7.1. Linear quenching

Fig. 6 shows the computed nucleation rates from quenching simulations at different constant cooling rates using the transient model. The

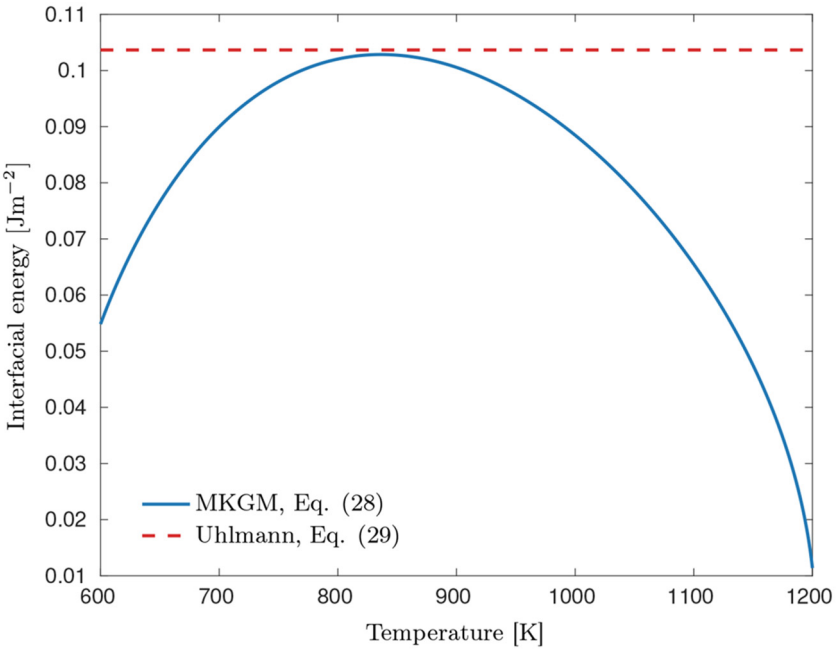

Fig. 5. Interfacial energy as a function of temperature. The temperature-dependent MKGM model given by Eq. (28) (blue solid line) and the constant value evaluated using Uhlmann's expression in Eq. (29) (red dashed line).

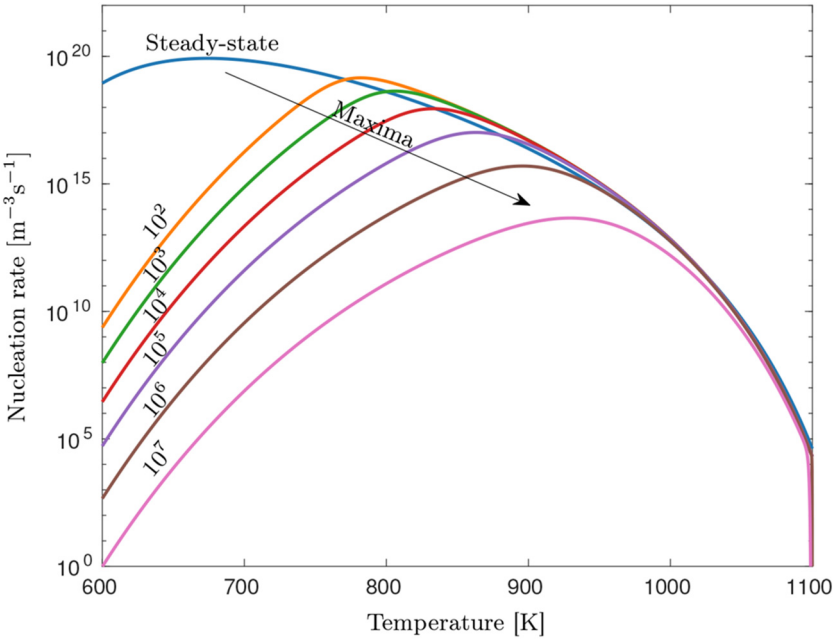

Fig. 6. Nucleation rate as a function of temperature for different cooling rates (Ks^{-1}). Increasing the cooling rate results in a slower nucleation rate and a shift in the maximum value to higher temperatures as indicated by the black arrow.

steady-state nucleation rate, computed using Eq. (9), has been included as reference. The transient simulation is initiated at $T = 1100$ K by assuming an initial steady-state cluster size distribution given by Eq. (12). The initial liquid is quenched to $T = 600$ K at the chosen cooling rate and the transient nucleation rate is computed using Eq. (8). The temperature dependent interfacial energy given by Eq. (28) has been used in the simulations. In Fig. 6 it is shown that the quench introduces transient effects, which impairs the evolution of the cluster size distribution and prohibits it from developing into a steady-state distribution at each temperature. As a consequence, the nucleation rate becomes several orders of magnitude lower than the steady-state nucleation rate, especially at lower temperatures. The transient effects become more significant at higher cooling rates, not only decreasing the nucleation rate but also causing a shift of the peak value to higher temperatures.

The number of nuclei computed using Eq. (17) is presented in Fig. 7. The results show that transient nucleation cannot be ignored when the material is subjected to high cooling rates. This is manifested by the large difference in the number of nuclei produced at the end of the simulation. In the case of steady-state nucleation, the number of nuclei reaches $8 \cdot 10^{20}$ m^{-3} while in the case of transient nucleation at quench rates of 10^2 Ks^{-1} and 10^7 Ks^{-1} it becomes $8 \cdot 10^{18}$ m^{-3} and

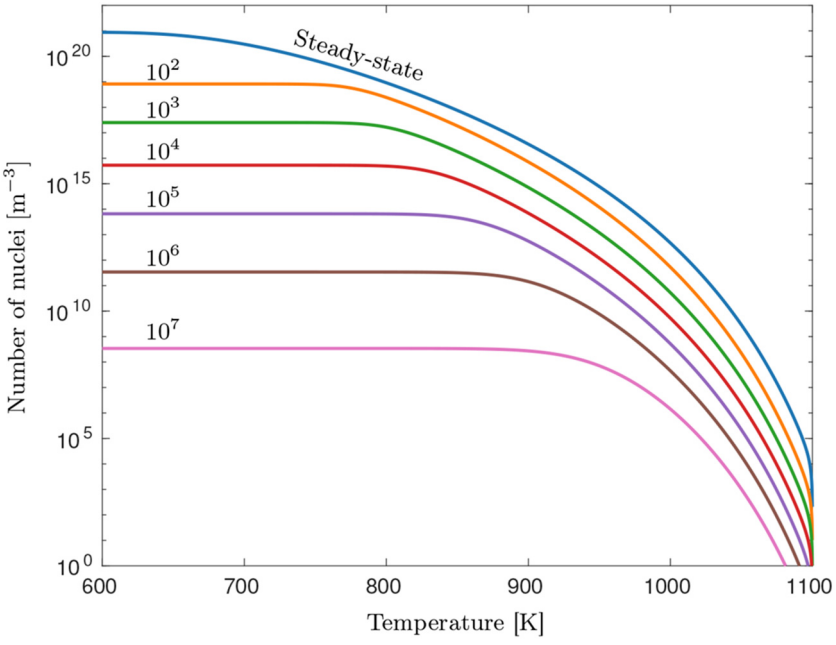

Fig. 7. The number of nuclei formed as a function of temperature at different cooling rates (Ks^{-1}). The numbers correspond to the nucleation rate shown in Fig. 6. A considerable decrease in nuclei formation is observed at higher cooling rates.

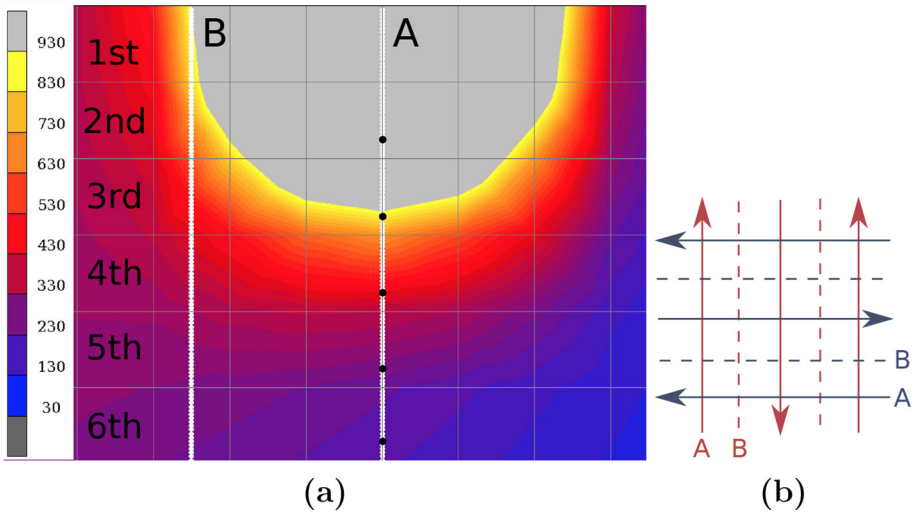

Fig. 8. (a) The temperature distribution in °C at the instant when the laser passes the cross section of the data extraction points. The laser power is 105 W. Each layer is numbered from 1st to 6th counting from the top surface. The data extraction points in the build direction are shown as black dots along the white lines, A: centerline, B: half hatch distance. (b) A schematic illustration of the X-Y remelting scan strategy. The arrows and dashed lines illustrate the centerline and hatch distance of the laser scans during the deposition (red) and remelting (blue) of a layer. The intersections correspond to the scanning scenarios A-A, B-B and A-B.

$3 \cdot 10^8$ m^{-3}, respectively. This means a difference of two and 12 orders of magnitude, respectively, in comparison with the case of steady-state nucleation.

7.2. Additive manufacturing

FE simulations of the transient thermal field during SLM processing of AMZ4 are considered. A detailed description of the FE model is presented in [9,65]. A scanning speed of 2000 mms^{-1}, a hatching distance of 100 μm and a layer thickness of 20 μm as proposed by Marattukalam et al. [31] for SLM processing of AMZ4 are utilized. The FE model is used to simulate the build of one layer on a AMZ4 substrate using four different laser powers: 75, 85, 95 and 105 W. The temperature profile is extracted within each layer across the build direction and is used to construct artificial temperature histories for the CNT models. The artificial temperature history is constructed by adding the temperature profile from each layer in a consecutive order starting from the top surface. The method is a valid representation, provided that the time between each layer deposition is long enough, which in the present case is 10 s based on measurements of the temperature in the build plate. The results from the thermal FE simulations and the measurements indicate that 10 s is sufficient for the heat accumulation to be negligible during the build process. To reproduce the X-Y remelting scan strategy

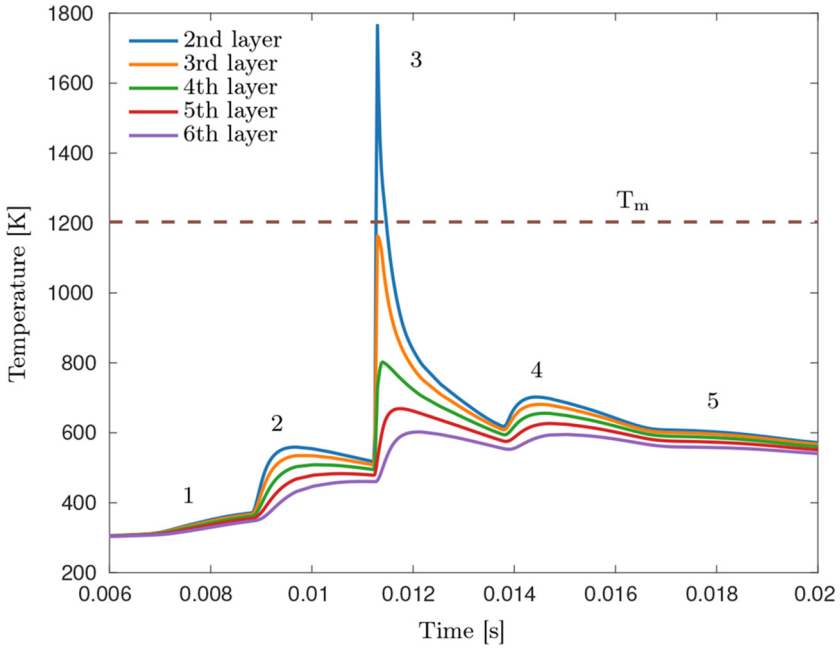

Fig. 9. Temperature in each layer as a function of time as obtained from the thermal simulation using a laser power of 105 W. The temperature is extracted from the black dots along line A in Fig. 8(a). The peaks numbered 1, 2, 4 and 5 corresponds to heating caused by previous and subsequent laser scans, while peak number 3 correspond to the laser crossing the data extraction point. The melting temperature T_m is indicated by the horizontal dashed line.

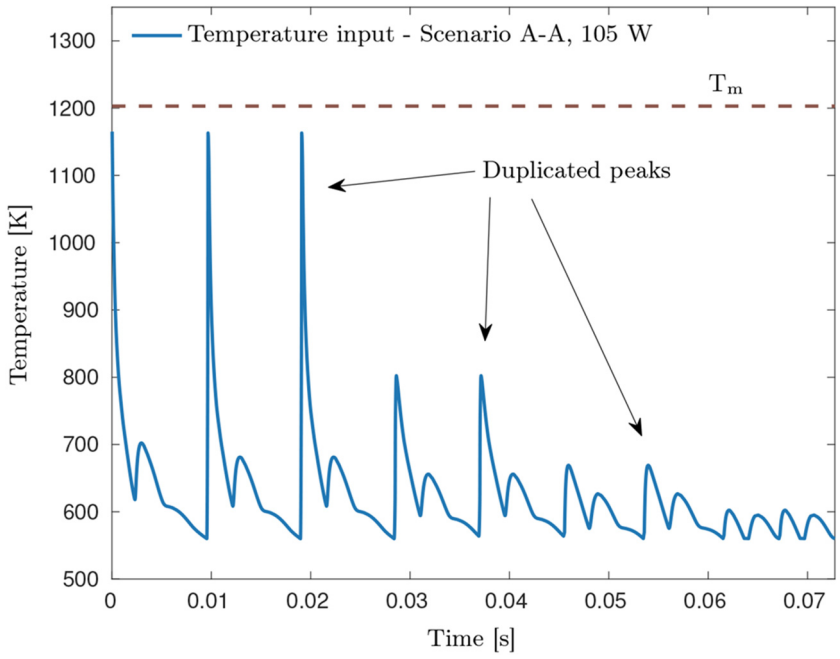

Fig. 10. Temperature history for scenario A-A using a laser power of 105 W. The data is created using the temperature history experienced by each layer (Fig. 9) and has been cut as the temperature drops below a threshold value of $T = 560$ K. The melting temperature T_m is indicated by the horizontal dashed line.

employed in [31], in which each layer is remelted once, the temperature history in each layer is duplicated depending on the scanning sequence. The remelting scan strategy is employed in the SLM process to increase the chemical homogeneity and to reduce the porosity of the printed part [5]. The constructed temperature histories are a representative for the complete temperature history experienced by a single layer and includes the effect of multiple scans and layer depositions.

Fig. 8(a) illustrates the temperature distribution in a cross section of the build using a laser power of 105 W. The temperature distribution is shown at the instant when the laser passes through the cross section and the grey region marks the region where $T > T_m$, i.e. the cross section of the melt pool. The temperature is extracted as a function of time across the build direction at the centre of and at half the hatch distance from the melt pool as indicated by the white lines A and B in Fig. 8. The data extracted from the black dots along line A is presented in Fig. 9 and is used to construct the artifical temperature history caused by multiple layer depositions seen in Fig. 10. The same procedure is used to create temperature histories for three different scenarios of the

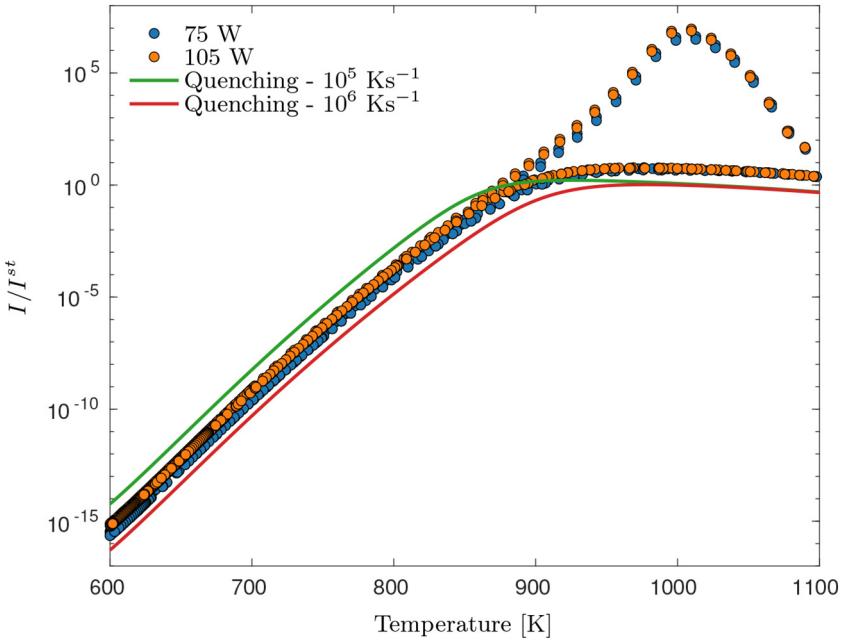

Fig. 11. Computed ratio of the transient nucleation rate to the steady-state nucleation rate as a function of temperature for scenario A-A. The temperature data in Fig. 10 is used for the 105 W simulation. The results from the quenching simulations using a cooling rate of 10^5 Ks^{-1} and 10^6 Ks^{-1} in Section 7.1 are included for reference.

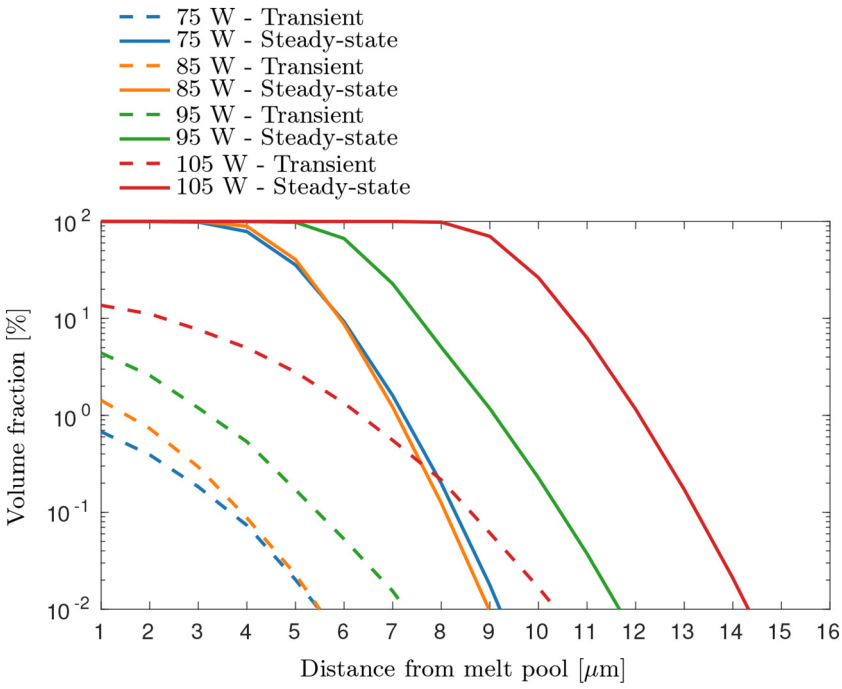

Fig. 12. Crystalline volume fraction across the layer thickness for scenario A-A.

X-Y remelting scan strategy illustrated in Fig. 8(b): A-A corresponding to the situation presented in Fig. 10, where the remelting scan passes the centerline A twice at the same relative position as the first scan; B-B is the same scanning procedure but instead across line B, located at half the hatch distance. Scenario B-B is of interest since the zone is subjected to the multipass effect [66]. The last scenario A-B, is the scanning scenario where the first scan passes line A and the second scan passes line B, which occurs since the remelting scan is rotated 90° relative the deposition scan. These temperature histories are used as input to the CNT model in which the simulations are initiated with a steady-state cluster size distribution equivalent to that at $T = 1166$ K.

The computed ratio of the transient nucleation rate to the steady-state nucleation rate of a location experiencing reheating in immediate proximity to the melt pool is presented in Fig. 11 for scenario A-A. Similar curves were obtained for scenarios B-B and A-B. The difference between the computed steady-state and transient nucleation rate is significant. At lower temperatures the transient nucleation rate is up to 15 orders of magnitude lower than the steady-state rate, which is a result from the quenched-in cluster size distribution caused by the high cooling rate. The deviation from the steady-state distribution during cooling seems to appear around $T \approx 890$ K depending on the laser power. The deviation is comparable to the results from Section 7.1 and seems to be equivalent to a cooling rate on the order of $10^5 - 10^6$ Ks^{-1}, which is reasonable considering that the average cooling rate of the temperature input is $5.9 \cdot 10^5$ Ks^{-1} for 75 W and $3.9 \cdot 10^5$ Ks^{-1} for 105 W, respectively. On heating, the quenched-in cluster size distribution is maintained and does not evolve into a steady-state cluster size distribution at increasing temperatures. This is evident from the overshoot in the nucleation rate shown at elevated temperatures in Fig. 11. The results from the simulations clearly suggest that the nucleation rate is time dependent in the AM processing of AMZ4 by SLM.

The computed crystalline volume fraction across the layer thickness, obtained when using different laser powers for scenario A-A, is presented in Fig. 12. The crystalline volume fraction is highest at the location experiencing reheating in immediate proximity to the melt pool and gradually decreases with increasing depth, demonstrating a distinct HAZ. The HAZ is significantly wider and has a higher fraction of crystals in the case of the steady-state nucleation model, suggesting that fully crystallized regions should be present in the as-built material for laser powers between 75 and 105 W. This is in contrast to the transient nucleation model, which predicts a partially crystalline HAZ in which the volume fraction increases with increasing laser power. The prediction of a partial crystalline HAZ is in agreement with SEM analysis of AMZ4 processed by SLM [31]. The SEM images reveal crystals embedded in an amorphous matrix as seen in Fig. 13. The crystals were clustered in regions, forming banded HAZ regions of a few μm in characteristic width. The size of the crystals were estimated to be 0.05 to 0.40 μm,

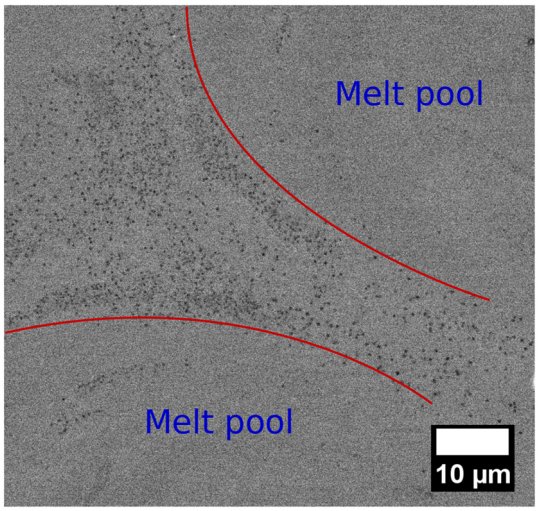

Fig. 13. SEM image of AMZ4 processed by SLM using a laser power of 75 W [31]. A partially crystalline HAZ can be observed close to the borders of the melt pools indicated by the red lines. The build direction is in the out-of-plane direction.

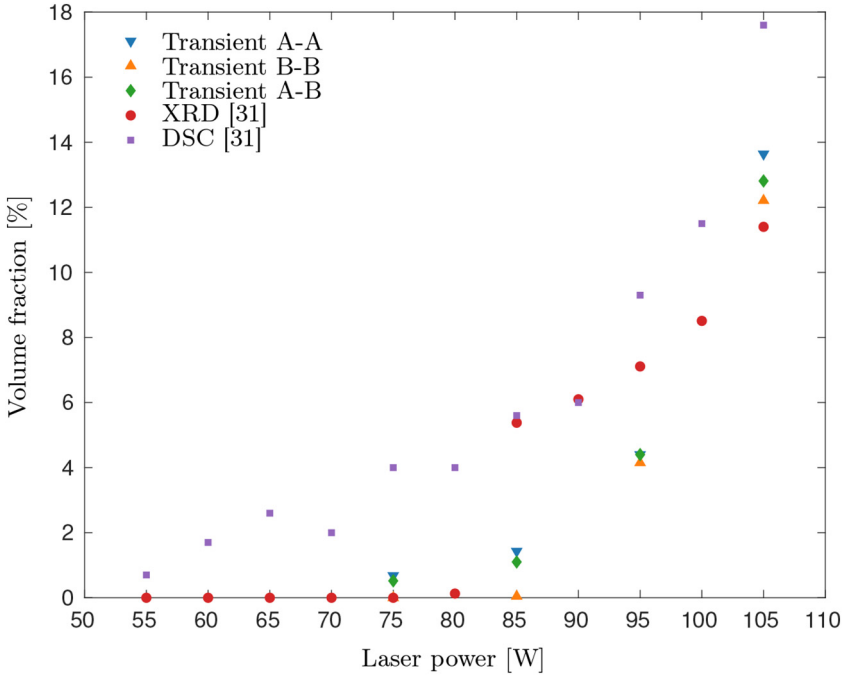

Fig. 14. The maximum crystalline volume fraction as a function of laser power for the different remelting scenarios (A-A, B-B, A-B), obtained using the transient model, compared to experimental data from [31].

which is smaller but comparable to the calculated mean radius based on the transient simulations between 0.03 and 1.64 μm, depending on laser power and scanning scenario. Observations of partially crystalline HAZ regions have also been made in other studies involving laser processing of Zr-based BMGs [5,15,20,67]. In the study by Li et al. [5], SLM processing of a $Zr_{52.2}Ti_5Cu_{17.9}Ni_{14.6}Al_{10}$ (at%) BMG resulted in amorphous or partial crystalline samples using laser energy densities below 27 Jmm^{-3} (calculated as $E_p = \frac{P}{Vht}$ where P is the laser power, h is the hatching distance, t is the layer thickness, V is the laser scan speed). The observation is in agreement with the results from the present study, in which the laser powers between 75 and 105 W correspond to laser energy densities between 18.75 and 26.25 Jmm^{-3}.

The crystalline volume fraction of AMZ4 manufactured by SLM has been estimated using XRD and DSC by Marattukalam et al. [31]. Cylindrical samples were manufactured with laser powers raging from 55 W to 105 W in steps of 5 W. The laser spot

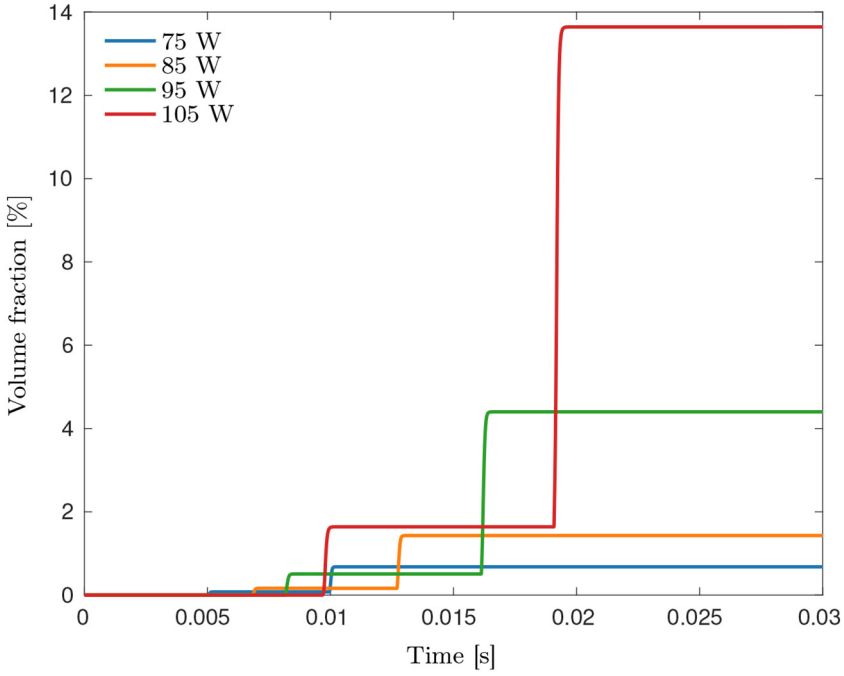

Fig. 15. Crystalline volume fraction as a function of time for scenario A-A using different laser powers. The major crystallization events occur during the deposition and remelting of the second consecutive layer, as a result of the temperature peaks presented in Fig. 16.

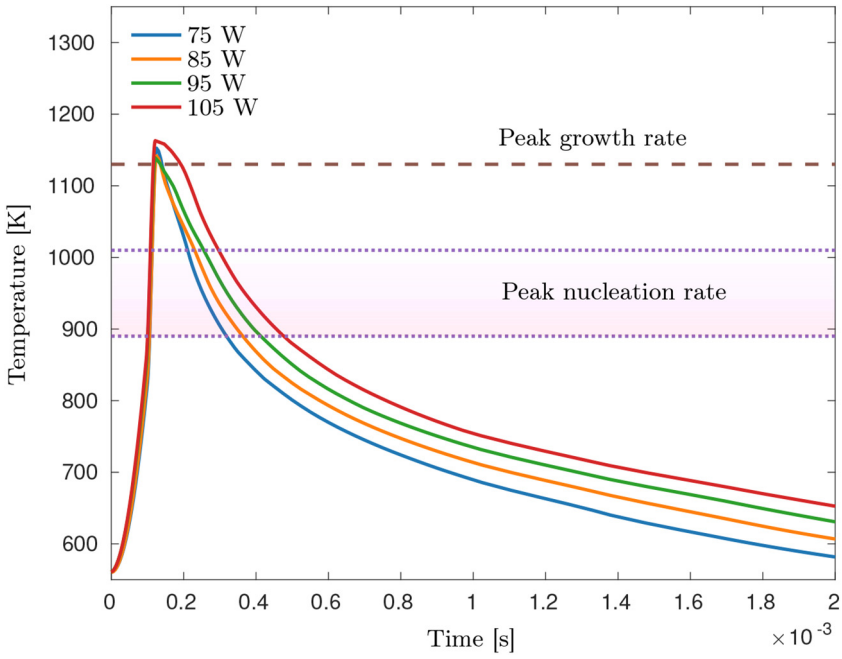

Fig. 16. Comparison of the thermal peaks caused by the second consecutive layer addition in scenario A-A for different laser powers. The dashed line marks the peak growth rate. The faded zone illustrates the temperature range of the peak transient nucleation rate.

diameter (40 μm), the scan speed (2000 mms^{-1}), hatch spacing (100 μm), layer thickness (20 μm) and X-Y remelting scan strategy were kept constant for these samples. For laser powers at and below 80 W, the diffraction patterns of the printed samples closely resembled those of the amorphous powder, while crystalline diffraction peaks were present at laser powers above 80 W. The computed crystalline volume fraction from the experimental analysis is presented together with the results from the transient simulations in Fig. 14. The calculated volume fraction based on the transient simulations are of comparable magnitude to those obtained from the experimental analysis and follow the same trend with respect to the applied laser power. A diminishing volume fraction is observed at laser powers below 80 W for all scenarios A-A, B-B and A-B, which is in agreement with the results from the XRD analysis. A comparison with the results from the steady-state nucleation model shown in Fig. 12, suggest that the transient nucleation model provides a better prediction of the crystallinity resulting from the SLM process than the steady-state model.

The diminishing volume fraction at lower laser powers can be explained by examining the volume fraction as a function of time as shown in Fig. 15. Independent of the applied laser power, the major crystallization events occurs when the laser reheats the material due to the deposition and remelting of the second consecutive layer (labeled "3rd layer" in Figs. 8(a) and 9). An increase is observed at all laser powers but with varying increase in volume fraction. The increase in volume fraction is directly related to the time the material is exposed to critical temperatures where the nucleation and growth rate is higher. The temperature peak of the second consecutive layer deposition for scenario A-A is shown in Fig. 16 for different laser powers. At a decreasing laser power, the cooling rate becomes higher and the material is exposed to higher nucleation and growth rates for a shorter duration, hence resulting in less crystallization as shown in Fig. 15.

8. Conclusions

A numerical model of transient nucleation, based on CNT, is established and employed to study transient nucleation effects during SLM processing of a Zr-based BMG. The model is calibrated using JMAK theory against an experimentally obtained TTT-diagram from DSC measurements performed on AMZ4 bulk metallic glass ($Zr_{59.3}Cu_{28.8}Al_{10.4}Nb_{1.5}$ (at%)). The following observations are made:

- Model calibration using the temperature dependent expression of the interfacial energy proposed by Mondal et al. [52], provides a good agreement with the experimentally obtained TTT-diagram. The convincing agreement is a direct consequence of removing any assumption of a temperature independent interfacial energy.
- Time dependent simulations of nucleation and growth are performed by adopting the temperature histories from a thermal finite element simulation of selective laser melting of AMZ4 as model input. The numerical simulations show that the high heating and cooling rates in the SLM process induce transient nucleation effects, which shift the value of the nucleation rate by up to 15 orders of magnitude below the steady-state nucleation rate on cooling and up to seven orders of magnitude above the steady-state nucleation rate on heating. The large difference in the nucleation rate clearly indicates that the steady-state assumption of nucleation does not hold for AMZ4 under SLM processing conditions.
- Evaluation of the crystalline volume fraction across the layer thickness using the transient model reveals a partially crystallized HAZ with varying crystalline volume fraction. The crystalline volume fraction is highest at the location experiencing reheating in immediate proximity to the melt pool.
- The calculated crystalline volume fraction in the HAZ region is presented as function of applied laser power. As expected, the volume fraction decreases with decreasing laser power. The model predicts a diminishing crystalline volume fraction at laser powers below 80 W, which has been confirmed experimentally through XRD analysis. The crystalline volume fractions calculated based on the transient model are in agreement with experimentally determined volume fractions in SLM-processed AMZ4.

These findings, along with the proposed modelling strategy, provide tools that can be used to further develop techniques and processing conditions for SLM processing of AMZ4.

Data availability

The data required to reproduce these findings cannot be shared at this time as the data also forms part of an ongoing study.

Declaration of Competing Interest

The authors declare that they have no known competing financial interests or personal relationships that could have appeared to influence the work reported in this paper.

Acknowledgements

This work was carried out with financial support from the Swedish Foundation for Strategic Research (SSF), through the project Additive Manufacturing - Development of Process and Material [grant number GMT14-0048]; the strategic innovation program LIGHTer provided by Sweden's Innovation Agency [grant number 2017-05200]; and from the Swedish Foundation for Strategic Research (SSF) within the Swedish national graduate school in neutron scattering (SwedNess), which are gratefully acknowledged. The authours wish to thank Moritz Stolpe and Heraeus Additive Manufacturing GmbH for providing the samples used in the DSC study. The authors wish to thank Sebastian König for his help with the low temperature DSC measurements and Sebastian Östlund, Dr. Juergen Schawe and Mettler Toledo for conducting the calorimetry measurements using the Flash DSC2+. The authors also wish to thank Jithin Marattukalam and Dennis Karlsson for providing the image from the SEM analysis of SLM-processed AMZ4 (Fig. 13).

References

[1] M.F. Ashby, A.L. Greer, Metallic glasses as structural materials, Scr. Mater. 54 (3) (2006) 321–326, https://doi.org/10.1016/j.scriptamat.2005.09.051.
[2] A. Inoue, X.M. Wang, W. Zhang, Developments and applications of bulk metallic glasses, Rev. Adv. Mater. Sci. 18 (2008) 1–9.
[3] C. Suryanarayanam, A. Inoue, Bulk metallic glasses, first ed. CRC Press, Boca Raton, 2011.
[4] C. Zhang, X.-M. Li, S.-Q. Liu, H. Liu, L.-J. Yu, L. Liu, 3D printing of Zr-based bulk metallic glasses and components for potential biomedical applications, J. Alloys Compd. 790 (2019) 963–973, https://doi.org/10.1016/j.jallcom.2019.03.275.
[5] X.P. Li, M.P. Roberts, S. O'Keeffe, T.B. Sercombe, Selective laser melting of Zr-based bulk metallic glasses: processing, microstructure and mechanical properties, Mater. Des. 112 (2016) 217–226, https://doi.org/10.1016/j.matdes.2016.09.071.
[6] E. Williams, N. Lavery, Laser processing of bulk metallic glass: a review, J. Mater. Process. Technol. 247 (March) (2017) 73–91, https://doi.org/10.1016/j.jmatprotec.2017.03.034.
[7] Z. Mahbooba, L. Thorsson, M. Unosson, P. Skoglund, H. West, T. Horn, C. Rock, E. Vogli, O. Harrysson, Additive manufacturing of an iron-based bulk metallic glass larger than the critical casting thickness, Appl. Mater. Today 11 (2018) 264–269, https://doi.org/10.1016/j.apmt.2018.02.011.
[8] G. Yang, X. Lin, F. Liu, Q. Hu, L. Ma, J. Li, W. Huang, Laser solid forming Zr-based bulk metallic glass, Intermetallics 22 (2012) 110–115, https://doi.org/10.1016/j.intermet.2011.10.008.
[9] J. Lindwall, V. Pacheco, M. Sahlberg, A. Lundbäck, L.-E. Lindgren, Thermal simulation and phase modeling of bulk metallic glass in the powder bed fusion process, Addit. Manuf. 27 (March) (2019) 345–352, https://doi.org/10.1016/j.addma.2019.03.011.
[10] D.C. Hofmann, J.-Y. Suh, A. Wiest, G. Duan, M.-L. Lind, M.D. Demetriou, W.L. Johnson, Designing metallic glass matrix composites with high toughness and tensile ductility, Nature 451 (28) (2008) 1085–1089, https://doi.org/10.1038/nature06598.
[11] Y. Wu, H. Wang, H.H. Wu, Z.Y. Zhang, X.D. Hui, G.L. Chen, X.L. Wang, Z.P. Lu, Formation of Cu–Zr–Al Bulk Metallic Glass Composites with Improved Tensile Properties, 59, 2011 2928–2936, https://doi.org/10.1016/j.actamat.2011.01.029.
[12] R.L. Narayan, P.S. Singh, D.C. Hofmann, N. Hutchinson, K.M. Flores, U. Ramamurty, On the microstructure-tensile property correlations in bulk metallic glass matrix composites with crystalline dendrites, Acta Mater. 60 (2012) 5089–5100, https://doi.org/10.1016/j.actamat.2012.06.032.
[13] K. Kosiba, S. Scudino, R. Kobold, U. Kühn, A.L. Greer, J. Eckert, S. Pauly, Transient nucleation and microstructural design in flash-annealed bulk metallic glasses, Acta Mater. 127 (2017) 416–425, https://doi.org/10.1016/j.actamat.2017.01.059.
[14] H.D. Vora, S. Mridha, S. Katakam, H.S. Arora, S. Mukherjee, N.B. Dahotre, Thermodynamics and kinetics of laser induced transformation in zirconium based bulk metallic glass, J. Non-Cryst. Solids 432 (2016) 237–245, https://doi.org/10.1016/j.jnoncrysol.2015.10.013.
[15] Y. Lu, H. Zhang, H. Li, H. Xu, G. Huang, Z. Qin, X. Lu, Crystallization prediction on laser three-dimensional printing of Zr-based bulk metallic glass, J. Non-Cryst. Solids 461 (2017) 12–17, https://doi.org/10.1016/j.jnoncrysol.2017.01.038.
[16] S. Karthika, T.K. Radhakrishnan, P. Kalaichelvi, A review of classical and nonclassical nucleation theories, Cryst. Growth Des. 16 (11) (2016) 6663–6681, https://doi.org/10.1021/acs.cgd.6b00794.
[17] K.F. Kelton, A.L. Greer, Test of classical nucleation theory in a condensed system, Phys. Rev. B 38 (14) (1988) 10089–10092, https://doi.org/10.1103/PhysRevB.38.10089.
[18] L. Gránásy, Quantitative analysis of the classical nucleation theory on glass- forming alloys, J. Non-Cryst. Solids 158 (1993) 514–518, https://doi.org/10.1016/0022-3093(93)90010-U.
[19] M. Fisk, A. Lundbäck, J. Edberg, J.M. Zhou, Simulation of microstructural evolution during repair welding of an IN718 plate, Finite Elem. Anal. Des. 120 (2016) 92–101, https://doi.org/10.1016/j.finel.2016.07.007.
[20] Y. Shen, Y. Li, H.L. Tsai, Evolution of crystalline phase during laser processing of Zr-based metallic glass, J. Non-Cryst. Solids 481 (November 2017) (2018) 299–305, https://doi.org/10.1016/j.jnoncrysol.2017.11.001.
[21] K.F. Kelton, A.L. Greer, C.V. Thompson, Transient nucleation in condensed systems, J. Chem. Phys. 79 (12) (1983) 6261–6276, https://doi.org/10.1063/1.445731.
[22] K.F. Kelton, A. Greer, Transient nucleation effects in glass formation, J. Non-Cryst. Solids 79 (1986) 295–309, https://doi.org/10.1016/0022-3093(86)90229-2.
[23] K.F. Kelton, Numerical model for isothermal and non-isothermal crystallization of liquids and glasses, J. Non-Cryst. Solids 163 (3) (1993) 283–296, https://doi.org/10.1016/0022-3093(93)91306-N.
[24] K.F. Kelton, Transient nucleation in glasses, Mater. Sci. Eng. B 32 (3) (1995) 145–151, https://doi.org/10.1016/0921-5107(95)80023-9.
[25] K. Kelton, A. Greer, Nucleation in Condensed Matter: Applications in Materials and Biology, first ed. Pergamon, Oxford, 2010 https://doi.org/10.1016/S1470-1804(09)01515-6.
[26] Material Data Sheet: AMZ4, https://www.heraeus.com/en/group/products_and_solutions_group/additive_manufacturing/metalpowders/metalpowders.html.
[27] V. Pacheco, D. Karlsson, J. Marattukalam, M. Stolpe, B. Hjörvarsson, U. Jansson, M. Sahlberg, Thermal stability and crystallization of a Zr-based metallic glass produced by suction casting and selective laser melting, J. Alloys Compd. 825 (2020) 153995, https://doi.org/10.1016/j.jallcom.2020.153995.
[28] B. Zhao, B. Yang, A. Abyzov, J. Schmelzer, J. Rodriguez-Viejo, Q. Zhai, C. Schick, Y. Gao, Beating homogeneous nucleation and tuning atomic ordering in glass-forming metals by nanocalorimetry, Nano Lett. 17 (2017) 7751–7760, https://doi.org/10.1021/acs.nanolett.7b03952.
[29] J. Schawe, J. Löffler, Existence of multiple critical cooling rates which generate different types of monolithic metallic glass, Nat. Commun. 10 (2019) 1–10, https://doi.org/10.1038/s41467-018-07930.
[30] Flash Differential Scanning Calorimetry (Flash DSC) METTLER TOLEDO, https://www.mt.com/hk/en/home/products/Laboratory_Analytics_Browse/TA_Family_Browse/Flash_DSC.html.
[31] J. Marattukalam, V. Pacheco, D. Karlsson, L. Riekehr, J. Lindwall, F. Forsberg, U. Jansson, M. Sahlberg, B. Hjörvarsson, Development of process parameters for selective laser melting of a Zr-based bulk metallic glass, Addit. Manuf. 33 (2020) 101124, https://doi.org/10.1016/j.addma.2020.101124.
[32] M. Volmer, A. Weber, Keimbildung in übersättigten Gebilden, Z. Phys. Chem. 119 (1926) 277–301, https://doi.org/10.1515/zpch-1926-11927.
[33] D.T. Wu, Nucleation theory, in: F. Ehrenreich, H. Spaepen (Eds.), Solid State Physics - Advances in Research and Applications, 50, Academic Press 1997, pp. 37–187, https://doi.org/10.1016/S0081-1947(08)60604-9.
[34] R. Becker, W. Döring, Kinetische behandlung der Keimbildung in übersättigten dämpfen, Ann. Phys. 24 (1935) 719–752, https://doi.org/10.1002/andp.19354160806.
[35] L.F. Shampine, M.W. Reichelt, The Matlab ODE suite, SIAM J. Sci. Comput. 18 (1997) 1–22, https://doi.org/10.1137/S1064827594276424.
[36] M. Perez, M. Dumont, D. Acevedo-Reyes, Implementation of classical nucleation and growth theories for precipitation, Acta Mater. 56 (9) (2008) 2119–2132, https://doi.org/10.1016/j.actamat.2007.12.050.
[37] A. Kolmogorov, On the statistical theory of metal crystallization, Izv. Akad. Nauk SSSR Ser. Mat. 3 (1937) 355–360, https://doi.org/10.1007/978-94-011-2260-3_22.
[38] W.A. Johnson, R.F. Mehl, Reaction kinetics in processes of nucleation and growth, Trans. AIME 135 (1939) 416–442, https://doi.org/10.1007/s11663-010-9421-1.
[39] M. Avrami, Kinetics of phase change. I general theory, J. Chem. Phys. 7 (1939) 1103–1112, https://doi.org/10.1063/1.1750380.
[40] J. Heinrich, R. Busch, B. Nonnenmacher, Processing of a bulk metallic glass forming alloy based on industrial grade Zr, Intermetallics 25 (2012) 1–4, https://doi.org/10.1016/j.intermet.2012.02.011.
[41] A. Einstein, Über die von der molekularkinetischen Theorie der Wärme geforderte Bewegung von in ruhenden Flüssigkeiten suspendierten Teilchen, Ann. Phys. 322 (8) (1905) 549–560.
[42] W. Sutherland, LXXV. A dynamical theory of diffusion for non-electrolytes and the molecular mass of albumin, Lond. Edinb. Dublin Philos. Mag. J. Sci. 9 (54) (1904) 781–785, https://doi.org/10.1080/14786440509463331.
[43] J. Brillo, A.I. Pommrich, A. Meyer, Relation between self-diffusion and viscosity in dense liquids: new experimental results from electrostatic levitation, Phys. Rev. Lett. 107 (16) (2011) 1–4, https://doi.org/10.1103/PhysRevLett.107.165902.
[44] D. Lee, B. Zhao, E. Perim, H. Zhang, P. Gong, Y. Gao, Y. Liu, C. Toher, S. Curtarolo, J. Schroers, J.J. Vlassak, Crystallization behavior upon heating and cooling in $Cu_{50}Zr_{50}$ metallic glass thin films, Acta Mater. 121 (2016) 68–77, https://doi.org/10.1016/j.actamat.2016.08.076.

[45] D. Lee, J.J. Vlassak, Diffusion kinetics in binary CuZr and NiZr alloys in the supercooled liquid and glass states studied by nanocalorimetry, Scr. Mater. 165 (2019) 73–77, https://doi.org/10.1016/j.scriptamat.2019.02.014.
[46] W. Hembree, High Temperature Rheology of Zr-Based Bulk Metallic Glass Forming Liquids, Doctorial thesis Universität des Saarlandes, 2015.
[47] M.E. Blodgett, T. Egami, Z. Nussinov, K.F. Kelton, Proposal for universality in the viscosity of metallic liquids, Sci. Rep. 5 (2015) 1–8, https://doi.org/10.1038/srep13837.
[48] F. Spaepen, A structural model for the solid-liquid interface in monatomic systems, Acta Metall. 23 (6) (1975) 729–743, https://doi.org/10.1016/0001-6160(75)90056-5.
[49] F. Spaepen, R.B. Meyer, The surface tension in a structural model for the solid-liquid interface, Scr. Metall. 10 (3) (1976) 257–263, https://doi.org/10.1016/0036-9748(76)90374-4.
[50] J.J. Hoyt, M. Asta, T. Haxhimali, A. Karma, R.E. Napolitano, R. Trivedi, B.B. Laird, J.R. Morris, Crystal-melt interfaces and solidification morphologies in metals and alloys, MRS Bull. 29 (2004) 935–939, https://doi.org/10.1557/mrs2004.263.
[51] J.J. Hoyt, S. Raman, N. Ma, M. Asta, Unusual temperature dependence of the solid-liquid interfacial free energy in the Cu-Zr system, Comput. Mater. Sci. 154 (2018) 303–308, https://doi.org/10.1016/j.commatsci.2018.07.050.
[52] K. Mondal, A. Kumar, G. Gupta, B.S. Murty, Temperature and structure dependency of solid-liquid interfacial energy, Acta Mater. 57 (11) (2009) 3422–3430, https://doi.org/10.1016/j.actamat.2009.03.051.
[53] D.R. Uhlmann, Crystallization and melting in glass-forming systems, in: T.J. Gray, V.D. Fréchette (Eds.), Kinetics of Reactions in Ionic Systems, Springer US, Boston, MA 1969, pp. 172–197.
[54] A. Masuhr, T.A. Waniuk, R. Busch, W.L. Johnson, Time scales for viscous flow, atomic transport, and crystallization in the liquid and supercooled liquid states of ZrTiCuNiBe, Phys. Rev. Lett. 61 (1988) 2291–2293, https://doi.org/10.1103/PhysRevLett.82.2290.
[55] X. Tang, U. Geyer, R. Busch, W. Johnson, Y. Wu, Diffusion mechanisms in metallic supercooled liquids and glasses, Nature 402 (1999) 160–162, https://doi.org/10.1038/45996.
[56] P. Bordeenithikasem, M. Stolpe, A. Elsen, D.C. Hofmann, Glass forming ability, flexural strength, and wear properties of additively manufactured zr-based bulk metallic glasses produced through laser powder bed fusion, Addit. Manuf. 21 (2018) 312–317, https://doi.org/10.1016/j.addma.2018.03.023.
[57] I. Jonas, W. Hembree, F. Yang, R. Busch, A. Meyer, Industrial grade versus scientific pure: Influence on melt properties, Appl. Phys. Lett. 112 (17) (2018) 1–5, https://doi.org/10.1063/1.5021764.
[58] X. Lin, W. Johnson, W. Rhim, Effect of oxygen impurity on crystallization of an undercooled bulk glass forming Zr-Ti-Cu-Ni-Al alloy, Mater. Trans. 38 (5) (1997) 473–477, https://doi.org/10.2320/matertrans1989.38.473.
[59] J. Eckert, N. Mattern, M. Zinkevitch, M. Seidel, Crystallization behavior and phase formation in Zr-Al-Cu-Ni metallic glass containing oxygen, Mater. Trans. 39 (6) (1998) 623–632.
[60] C.T. Liu, M.F. Chisholm, M.K. Miller, Oxygen impurity and microalloying effect in a Zr-based bulk metallic glass alloy, Intermetallics 10 (2002) 1105–1112, https://doi.org/10.1016/S0966-9795(02)00131-0.
[61] D. Kawase, A.P. Tsai, A. Inoue, T. Masumoto, Crystallization on supercooled liquid in metallic Zr-Cu-Al glasses, Appl. Phys. Lett. 62 (2) (1993) 137–139, https://doi.org/10.1063/1.109350.
[62] J.B. Qiang, W. Zhang, G.Q. Xie, A. Inoue, The effect of Ti, Nb, and Ta additions to ZrAlCu metallic glass on the crystallization and formation of the icosahedral phase, J. Mater. Res. 22 (4) (2007) 1093–1097, https://doi.org/10.1557/jmr.2007.0130.
[63] P. Drescher, K. Witte, B. Yang, R. Steuer, O. Kessler, E. Burkel, C. Schick, H. Seitz, Composites of amorphous and nanocrystalline Zr–Cu–Al–Nb bulk materials synthesized by spark plasma sintering, J. Alloys Compd. 667 (2016) 109–114, https://doi.org/10.1016/j.jallcom.2016.01.161.
[64] A. Ericsson, M. Fisk, H. Hallberg, Modeling of nucleation and growth in glass-forming alloys using a combination of classical and phase-field theory, Comput. Mater. Sci. 165 (2019) 167–179, https://doi.org/10.1016/j.commatsci.2019.04.008.
[65] J. Lindwall, A. Malmelöv, A. Lundbäck, L.E. Lindgren, Efficiency and accuracy in thermal simulation of powder bed fusion of bulk metallic glass, J. Miner. Metals Mater. Soc. 70 (8) (2018) 1598–1603, https://doi.org/10.1007/s11837-018-2919-8.
[66] J. Oliveira, T. Santos, R. Miranda, Revisiting fundamental welding concepts to improve additive manufacturing: from theory to practice, Prog. Mater. Sci. 107 (2020) 100590, https://doi.org/10.1016/j.pmatsci.2019.100590.
[67] D. Oyang, L. Ning, W. Xing, J. Zhang, L. Liu, 3D printing of crack-free high strength Zr-based bulk metallic glass composite by selective laser melting, Intermetallics 90 (2017) 128–134, https://doi.org/10.1016/j.intermet.2017.07.010.